PNAS RESEARCH ARTICLE | EVOLUTION ENVIRONMENTAL SCIENCES

Reactive oxygen species drove red lineage phytoplankton to displace green lineage phytoplankton during the Mesozoic

Yuxi Zhao[a], Man Tong[a,1], Li Tian[a], Genming Luo[a], Ping Li[a], Haijun Song[a], Zhong-qiang Chen[a], Shucheng Xie[a], Andreas Kappler[b], and Songhu Yuan[a,1]

Affiliations are included on p. 10.

Edited by Shuhai Xiao, Virginia Polytechnic Institute and State University, Blacksburg, VA; received August 7, 2025; accepted December 8, 2025

The great phytoplanktonic shift from green to red plastid lineage dominance in the early Mesozoic marks a primary producer revolution in marine ecosystems, facilitating the rise of modern ecosystems and impacting global carbon cycling and energy flows. The causes driving this evolutionary transition have been attributed to the changes in essential nutrients and the environmental crises of the Permian–Triassic mass extinction. Nonetheless, the underlying mechanisms driving this transition remain poorly understood. Here, we integrated culture experiments, molecular and physiological analyses, big data analysis, and phylogenomic dating analyses to uncover how environmental stresses influence algal physiology, thereby altering their evolutionary trajectories. We find that environmental and endogenous reactive oxygen species (ROS) collaboratively shape phytoplanktonic responses. The structural characteristics of red lineage phytoplankton enhance resistance to environmental ROS, facilitating physiological strategies that minimize endogenous ROS accumulation, thereby driving more adaptive evolutionary trajectories under environmental stresses in the early Mesozoic. The alignment of the turnover in diversification dynamics between the two lineages with paleoenvironmental shifts that triggered increased ROS production supports the role of ROS in driving this evolutionary transition. Our findings highlight ROS as a key underlying factor driving phytoplankton evolution, providing predictive insights into major biota–environment coevolutions throughout Earth's history.

reactive oxygen species | phytoplankton evolution | environmental stress | Mesozoic

Significance

Our research reveals that reactive oxygen species (ROS), reactive molecules produced during stress, played a key role in one of Earth's major evolutionary transitions: the rise of red lineage phytoplankton in the early Mesozoic. These organisms evolved better strategies to manage ROS, giving them a survival edge in harsh environments. This insight not only explains a major shift in ocean ecosystems and global carbon cycling but also suggests that ROS may be a universal mechanism linking environmental stress to long-term biological evolution. Understanding how life responds to ROS can help predict biological changes under modern challenges like climate change and pollution, offering a powerful lens through which to explore both the past and future of life on Earth.

Phytoplankton have been the lifeblood of the marine biosphere for over one billion years and are responsible for over 45% of Earth's annual net primary production (1). Yet, the dominant phytoplankton lineages supporting oceanic primary productivity have shifted markedly over geological time. During the Neoproterozoic and Paleozoic eras, productivity was largely driven by the green lineage, which arose through secondary endosymbiosis with a green algal (chlorophyte) ancestor, giving rise to groups such as the *Euglenophyta* and *Chlorarachniophyta* (2, 3). In contrast, modern oceans are dominated by the red lineage, which acquired plastids via a separate endosymbiosis with a red algal (rhodophyte) ancestor and includes haptophytes, dinoflagellates, and stramenopiles (3–5). The Mesozoic rise of the red lineage over its green counterpart marked a pivotal evolutionary transition that reshaped marine biodiversity and transformed global biogeochemical cycles (3), as exemplified by the radiation of heavily armored red lineage taxa, such as coccolithophorids (secreting calcite coccoliths) and diatoms (producing silica frustules), whose mineralized innovations enhanced organic carbon export to the deep ocean (6). Understanding the causes and mechanisms driving the evolutionary transition of phytoplankton is crucial for gaining insights into current and future marine biodiversity and global biogeochemical cycles. Although shifts in essential nutrients, such as phosphates and metal elements, along with environmental crises of the Permian–Triassic mass extinction, have been hypothesized as key drivers (3, 7, 8), the physiological responses of phytoplankton to environmental changes remain poorly understood, leaving a critical gap in identifying the intrinsic mechanisms underlying phytoplankton evolution.

Reactive oxygen species (ROS), mainly comprising $\bullet O_2^-$, H_2O_2, $\bullet OH$, and $^1O_2$, are recognized as key cellular responders to environmental stresses in modern biology (9). Environmental stresses, such as shifts in redox status, drastic temperature fluctuations, intensified UV radiation, and elevated heavy metal levels, can induce ROS production both in natural environments and within biotic cells through incomplete reduction or excitation of O_2 (10–14). The generated ROS play a dual role in vivo depending on their concentrations. At lower levels, ROS act as essential redox signals regulating gene expression, redirecting energy from growth toward acclimation or defense against environmental

Author contributions: M.T. and S.Y. designed research; Y.Z. performed research; Y.Z. analyzed data; and Y.Z., M.T., L.T., G.L., P.L., H.S., Z.-q.C., S.X., A.K., and S.Y. wrote the paper.

The authors declare no competing interest.

This article is a PNAS Direct Submission.

[1]To whom correspondence may be addressed. Email: tongman@cug.edu.cn or yuansonghu622@cug.edu.cn.

This article contains supporting information online at https://www.pnas.org/lookup/suppl/doi:10.1073/pnas.2521306123/-/DCSupplemental.

Published January 9, 2026.

stresses (15–17). When ROS levels exceed the physiological threshold values of organisms, they could have detrimental impacts on a large variety of cellular, physiological, and biochemical functions (18). To mitigate the negative effects of ROS, organisms have evolved a regulatory network comprising enzymatic and nonenzymatic antioxidant systems to keep the magnitude of ROS within cells at nondamaging levels (19). The dynamic homeostasis between ROS production and the antioxidant system determines the physiological responses of organisms to environmental stresses (19). Notably, environmental stressors that amplified ROS production were widespread during the Paleozoic–Mesozoic transition (20–22). Based on this, we propose that ROS may serve as a substantial link between environmental stress and physiological responses, ultimately driving the evolutionary transition of phytoplankton.

To test our hypothesis, we cocultivated model green lineage phytoplankton and red lineage phytoplankton in simulated seawater to investigate their responses to various environmental stresses. *Chlorella* sp. and the dinoflagellate *Symbiodinium* sp. were selected as model organisms representing the green and red lineages, respectively. These species were chosen based on their deep evolutionary histories and ubiquitous distribution in global marine ecosystems, making them ideal representatives for this study. The results showed that different environmental stresses impacted the physiological states of phytoplankton through a common ROS-mediated pathway, involving a collaborative contribution of environmental and endogenous ROS. The differing cell structures, antioxidant capacity, and energy allocation strategies of red and green lineage phytoplankton resulted in varied physiological responses to ROS. In addition, fossil records and molecular clock analysis further confirmed the turnover in diversification dynamics between the two lineages align with paleoenvironmental shifts that triggered increased ROS production, demonstrating the long-term driving role of ROS in algal succession. Thus, our findings provide key insights into the dynamics of phytoplankton evolution and assist in predicting their responses to future environmental changes.

Results

Red–Green Lineage Phytoplankton Shift under Different Environmental Stresses. We first evaluated the variation in the abundance ratio of red lineage phytoplankton (*Symbiodinium* sp.) to green lineage phytoplankton (*Chlorella* sp.) under various environmental stresses, starting with a ratio of 1.0 in all experiments. In the absence of additional stresses, *Chlorella* sp. dominated over time, with the *Symbiodinium* sp. to *Chlorella* sp. ratio decreasing to 0.07 after 46 d of cocultivation (Fig. 1*A*). However, 10 h of UV-B radiation weakened or even reversed the dominance of *Chlorella* sp. After 46 d of post–UV-B exposure at 66 kJ/m^2/d, the *Symbiodinium* sp. to *Chlorella* sp. ratio increased to as high as 8.25 (Fig. 1*A*). This shift was driven by contrasting responses of the two species to UV-B stress. Starting from equal initial densities (4×10^4 cells/mL), *Chlorella* sp. reached 1.7×10^6 cells/mL after 46 d without UV-B, but declined to 3.0×10^4 cells/mL following UV-B exposure at 66 kJ/m^2/d (*SI Appendix*, Fig. S1*A*). In contrast, *Symbiodinium* sp. increased from 1.1×10^5 to 2.5×10^5 cells/mL after UV-B exposure (*SI Appendix*, Fig. S1*B*), indicating a lineage-specific sensitivity to UV-B radiation. To justify this lineage advantage is a general phenomenon and not a contingency of a specific algal species and to test whether it would also appear in a more complex community setting, we cocultured four additional phytoplankton species, two red lineage phytoplankton (*Cyclotella meneghiniana* and *Thalassiosira pseudonana*) and two green lineage phytoplankton (*Dunaliella* sp. and *Nannochloropsis oceanica*), under 10 h of UV-B radiation. This coculture also resulted in a shift from two green to two red lineage phytoplankton dominance (*SI Appendix*, Fig. S2). Similar to UV-B radiation, Fe(II) oxidation also promoted red lineage dominance (*SI Appendix*, Fig. S3*A*). In contrast, other environmental stresses, such as high CO_2 concentrations, nutrient fluctuations, and changes in metal levels, did not alter the dominance of green lineage (*SI Appendix*, Fig. S3 *B–D*). Interestingly, increasing the temperature from 25 °C to 35 °C alone sustained and even enhanced *Chlorella* sp. dominance. However, when combined with UV-B radiation, the temperature increase intensified the shift from *Chlorella* sp. to *Symbiodinium* sp. dominance (Fig. 1*B*), suggesting that temperature functions primarily as an amplification factor rather than a direct driver of phytoplankton transition.

To test whether our findings from single-species experiments translate to a multispecies, we selected species richness as our key metric and conducted a large-scale biogeographical analysis. This analysis utilized 556,626 phytoplankton survey records, encompassing 1,821 distinct species (Fig. 1 *C* and *D*), from worldwide oceanographic databases. We then conducted correlation analyses between phytoplankton species richness and the corresponding sea surface UV intensity and temperature. Correlation analysis shows that when UV intensity exceeds approximately 70 to 75 kJ/m^2/d, red lineage species richness increases while green lineage species richness decreases (Fig. 1*E*), which aligns with the shift in phytoplankton dominance observed at 66 kJ/m^2/d in our experiments. Correlation analysis also reveals that when sea surface temperature (SST) surpasses 25 °C, red lineage species richness increases while green lineage declines (Fig. 1*F*). Given the ocean surface's exposure to UV radiation, these findings support our experimental results, demonstrating that temperature amplifies phytoplankton shifts under UV-B radiation, with 25 °C acting as a key threshold for triggering phytoplankton transitions.

Critical Role of ROS in Phytoplankton Shift under Environmental Stresses. To explore the role of ROS in phytoplankton shift, both environmental and endogenous ROS levels were measured under various stresses. Both UV-B radiation and Fe(II) oxidation led to significant accumulation of environmental ROS. UV-B radiation at 66 kJ/m^2/d produced up to 1,909 nM •OH over 10 h (Fig. 2*A*), and Fe(II) oxidation generated 241 nM •OH within 1 h (*SI Appendix*, Fig. S4). When the temperature increased from 25 °C to 35 °C, •OH production under 66 kJ/m^2/d UV-B radiation further increased to 2,316 nM (Fig. 2*A*). However, other environmental stresses that did not induce phytoplankton shift resulted in minimal environmental ROS accumulation (*SI Appendix*, Fig. S4). Notably, the *Symbiodinium* sp. to *Chlorella* sp. ratio exhibited a significant positive correlation with environmental ROS concentrations (Fig. 2*B*). The addition of environmental ROS quenchers completely inhibited phytoplankton shift under UV-B radiation (Fig. 2*C*), while the addition of exogenous ROS significantly promoted phytoplankton shift (Fig. 2*D*). These findings collectively support that environmental ROS is a key mediator through which environmental stress influences phytoplankton shift.

Furthermore, significant endogenous ROS signals were observed in phytoplankton cells exposed to UV-B radiation (Fig. 2 *E* and *F*) and environmental H_2O_2 (*SI Appendix*, Fig. S5), while negligible endogenous ROS signals were detected in other groups that did not induce phytoplankton shift (*SI Appendix*, Fig. S6). Notably, when exposed to the same level of UV-B radiation or environmental H_2O_2, *Symbiodinium* sp. cells exhibit significantly lower endogenous ROS levels compared to *Chlorella* sp. cells

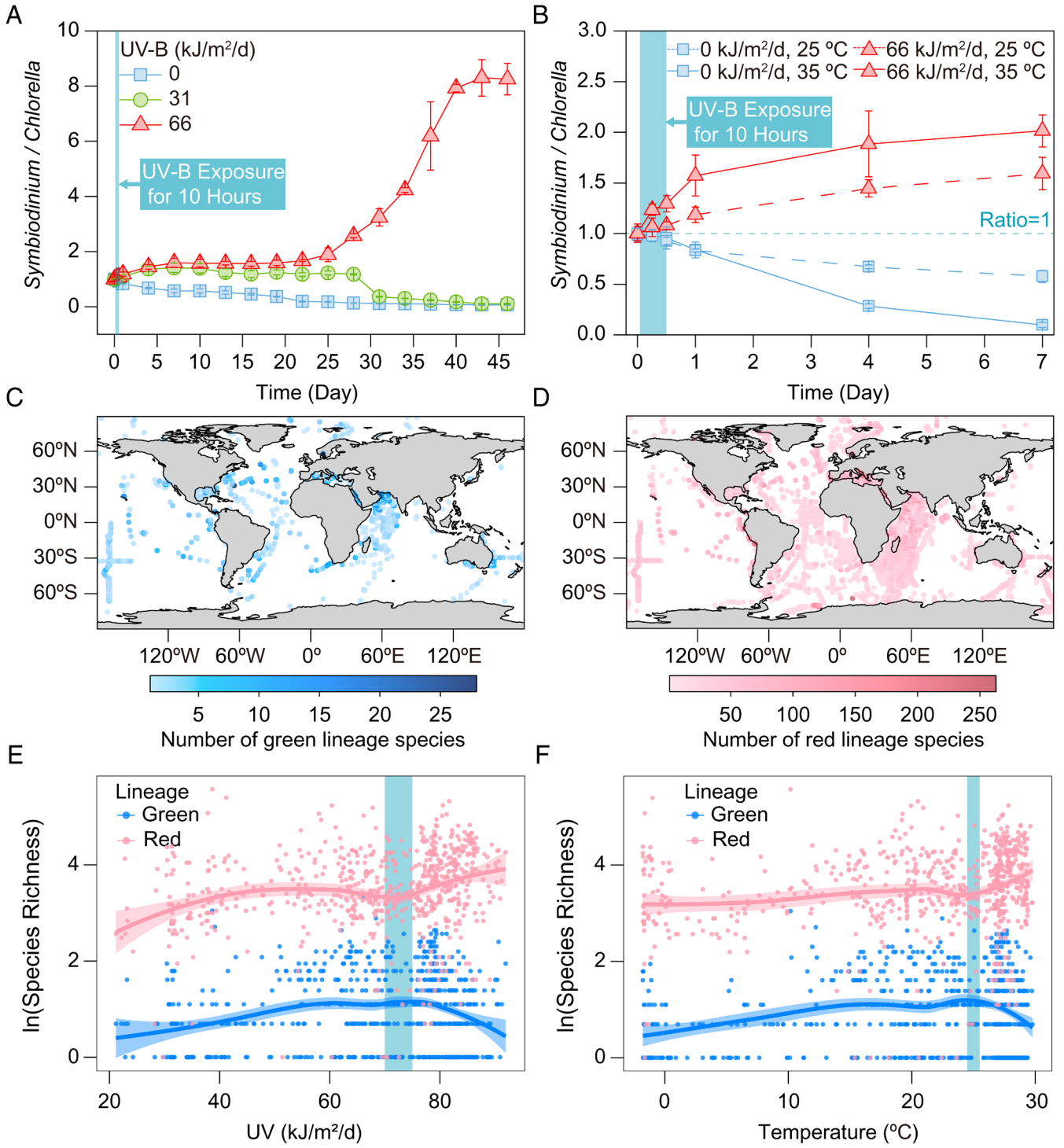

Fig. 1. Key environmental factors triggering the phytoplankton shift. (*A* and *B*) Effects of UV-B radiation (*A*) and temperature (*B*) on the abundance ratio of *Symbiodinium* sp. (red lineage) to *Chlorella* sp. (green lineage). Bars represent mean ± SD from three independent experiments. (*C* and *D*) Global marine distribution of species richness for green lineage (*C*) and red lineage (*D*) phytoplankton. Data represent the total species richness within each 1°×1° grid cell. (*E* and *F*), Correlation analysis between the species richness of red/green lineage phytoplankton and surface UV intensity (*E*) and surface temperature (*F*) in natural marine environments. The chosen phytoplankton dataset included six main phytoplankton phyla: *Chlorophyta*, *Euglenozoa*, *Ochrophyta*, *Cryptophyta*, *Haptophyta*, and *Myzozoa*, which are representative of major groups in marine phytoplankton.

(Fig. 2 *E* and *F* and *SI Appendix*, Fig. S5). This demonstrated an inverse relationship between endogenous ROS and the *Symbiodinium* sp. to *Chlorella* sp. ratio, suggesting that the reversal of growth advantage between *Symbiodinium* sp. and *Chlorella* sp. under the same environmental stress is likely related to their ability to manage ROS.

Cellular Structural Responses to ROS. To investigate the distinct response mechanisms of *Symbiodinium* sp. and *Chlorella* sp. to ROS, we characterized the cellular structural changes induced by UV-B radiation using transmission electron microscopy (TEM) and confocal laser scanning microscopy (CLSM). TEM images revealed that the *Symbiodinium* sp. cells had thicker cell walls

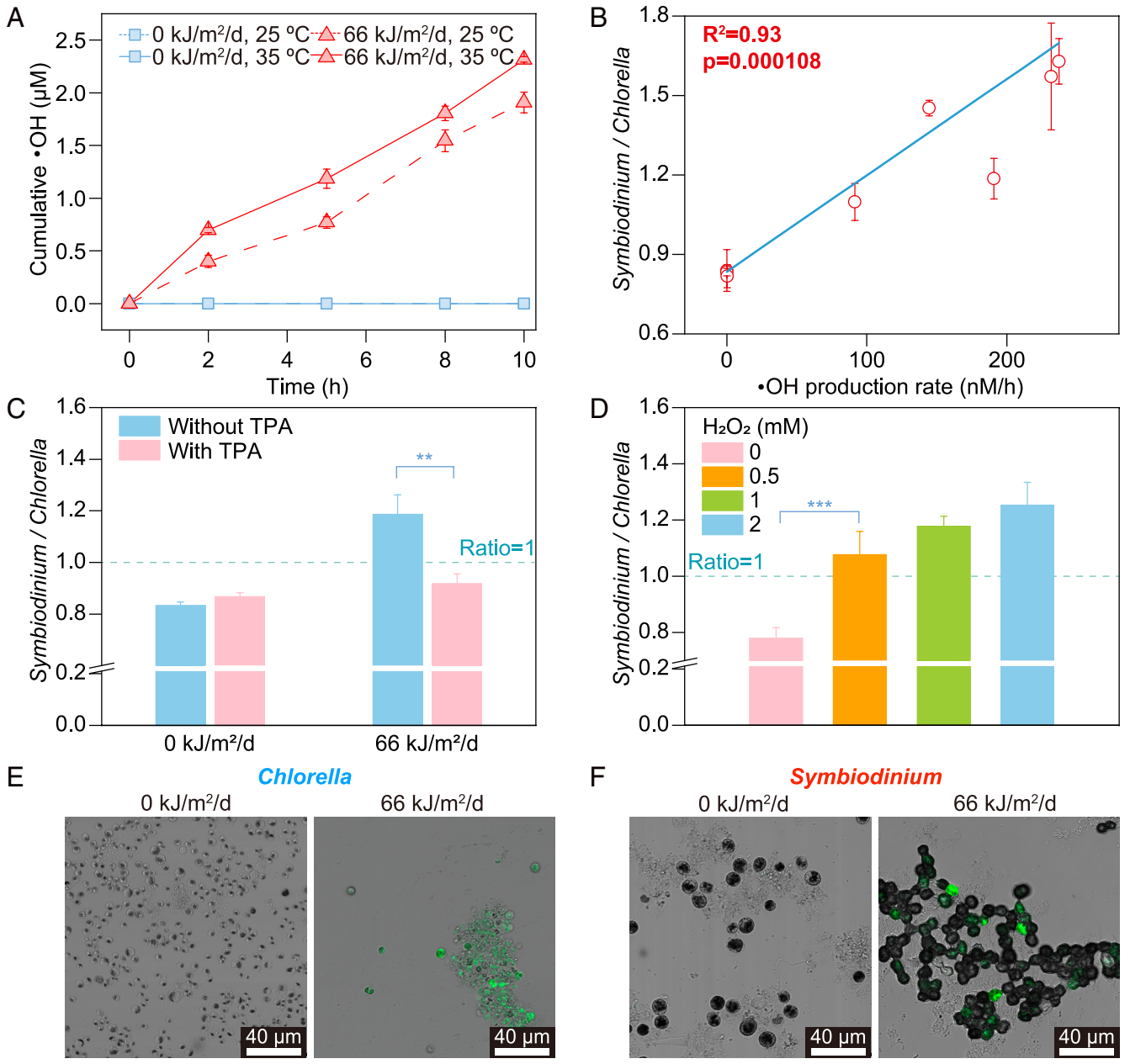

Fig. 2. Involvement of ROS in the dominance shift from *Chlorella* sp. (green lineage) to *Symbiodinium* sp. (red lineage) under environmental stresses. (*A*) Accumulation of •OH under UV-B radiation in the coculture. (*B*) Linear correlation between •OH production rate and the ratio of *Symbiodinium* sp. to *Chlorella* sp. (*C*) Effect of ROS quencher on the ratio of *Symbiodinium* sp. to *Chlorella* sp. under UV-B radiation. (*D*) Effect of exogenous H_2O_2 on the ratio of *Symbiodinium* sp. to *Chlorella* sp. lineage. (*E* and *F*) Fluorescence microscopy images of endogenous ROS signals in *Chlorella* sp. and *Symbiodinium* sp. under 10 h of UV-B radiation. Green fluorescence presents endogenous ROS concentrations. For panels (*A*), (*C*), and (*D*), symbols represent the mean ± SD from four independent experiments (N = 4). For panel *B*, N = 3 or 4, corresponding to the respective experimental groups. Statistical analysis in (*B*) was performed using weighted linear regression, with R^2 calculated as 1 minus the ratio of weighted residual sum of squares to weighted total sum of squares, and *P*-values derived from t-statistics of regression coefficients. Statistical analysis in (*C*) was performed using an unpaired two-tailed *t* test; significance is represented as $^{**}P < 0.01$ and $^{***}P < 0.001$.

compared to the *Chlorella* sp. (Fig. 3 *A* and *B*), a characteristic commonly observed across various red and green lineage phytoplankton species (23, 24). Under UV-B radiation, the cell walls of *Chlorella* sp. were visibly ruptured (Fig. 3*C*), while the cell walls of *Symbiodinium* sp. remained intact (Fig. 3*D*). CLSM images showed that after 10 h of UV-B radiation, the extracellular polymeric substances (EPS) of *Chlorella* sp. significantly decreased (Fig. 3*E*), while the EPS of *Symbiodinium* sp. remained abundant and formed aggregates (Fig. 3*F*). It has been reported that red lineage secreted EPS with a higher content of sulfated polysaccharide structures, which can significantly enhance their antioxidant activity (25). Therefore, the thicker cell wall of red lineage cells, along with their enhanced EPS antioxidant capacity and aggregation strategy, create a robust defense barrier, enhancing their resistance to oxidative stress induced by ROS.

Molecular Mechanisms of ROS-Driven Phytoplankton Shift. Transcriptome analysis demonstrated that after 10 h of UV-B exposure, lipid oxidation-related genes were significantly upregulated in *Chlorella* sp. but remained unchanged in *Symbiodinium* sp. (Fig. 4*A*), indicating greater *Symbiodinium* sp. resistance to ROS-induced structural damage, as lipid oxidation is a major pathway through which ROS disrupt cell membrane integrity (18, 26). Additionally, UV-B exposure upregulated photosynthesis-related

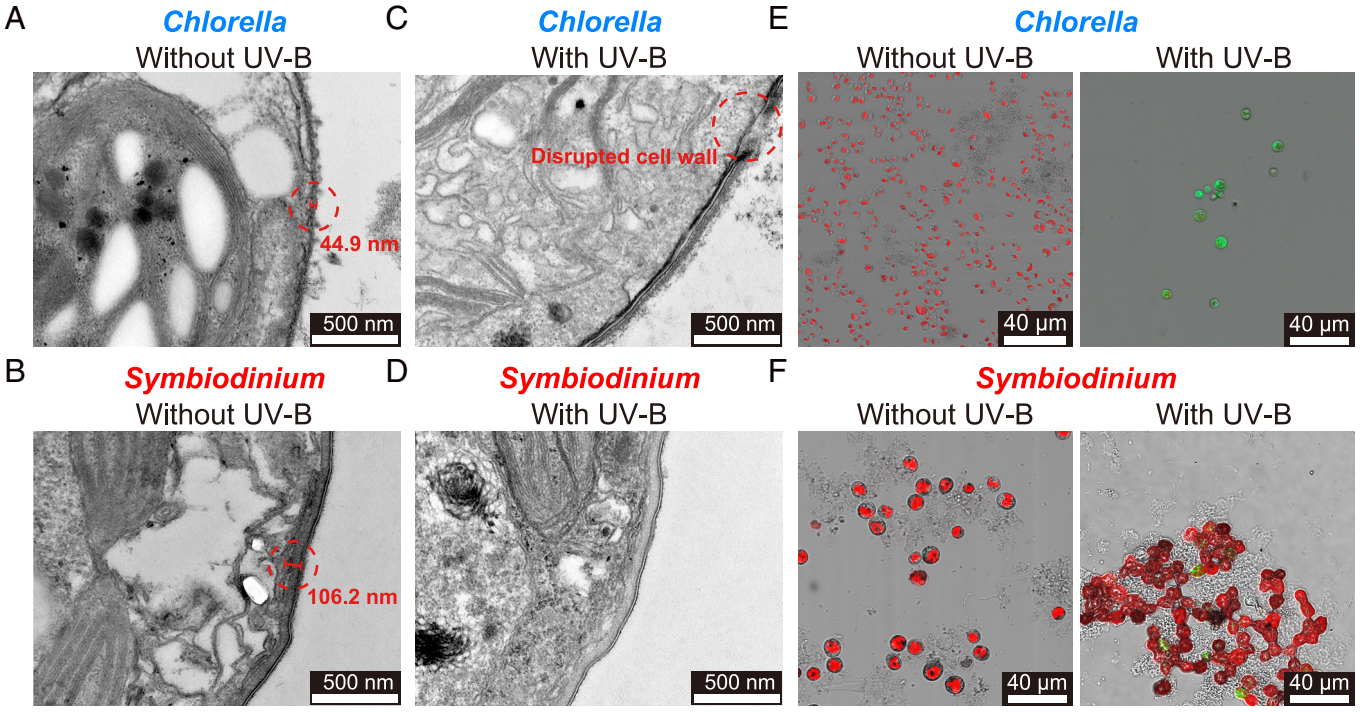

Fig. 3. Different cellular structural responses of *Symbiodinium* sp. (red lineage) and *Chlorella* sp. (green lineage). (*A* and *B*) TEM images of the cell wall structures of *Chlorella* sp. and *Symbiodinium* sp. (*C* and *D*) TEM images of the cell wall integrity of *Chlorella* sp. and *Symbiodinium* sp. under UV-B exposure. UV-B radiation was applied at a dose of 66 kJ/m^2/d over a 10-h photoperiod. (*E* and *F*) CLSM images showing variations in EPS of *Chlorella* sp. and *Symbiodinium* sp. under UV-B exposure, with red fluorescence indicating polysaccharides in the EPS and cell walls, and green fluorescence indicating intracellular ROS.

genes in *Chlorella* sp. but downregulated them in *Symbiodinium* sp. (Fig. 4*B*), suggesting that structural differences drove divergent metabolic strategies. *Chlorella* sp. adopted an energy-intensive response to meet the increased demands for defense and cell wall repair, whereas *Symbiodinium* sp. was able to conserve energy due to their structural integrity. Given that photosynthesis inevitably produces endogenous ROS via electron leakage (27), *Symbiodinium* sp. energy-conserving strategy helps limit endogenous ROS accumulation, whereas the increased photosynthetic activity in *Chlorella* sp. may intensify the accumulation. Furthermore, proteomic analysis revealed that *Symbiodinium* sp. upregulated PsaC, a protein containing Fe-S clusters essential for stabilizing the electron transport chain and minimizing electron leakage (28, 29), whereas *Chlorella* sp. exhibited reduced expression (Fig. 4*C*). Collectively, *Symbiodinium* sp.'s energy-conserving strategy and stable electron transport system contribute to their lower endogenous ROS levels (Fig. 2 *E* and *F*).

The production of endogenous ROS triggers antioxidant defenses to help mitigate oxidative damage (30, 31). Transcriptomic analysis showed that after 7 d of recovery from 10 h of UV-B exposure, antioxidant-related genes were significantly upregulated in *Symbiodinium* sp. but mostly downregulated in *Chlorella* sp. (Fig. 4 *D*–*F*), indicating a stronger ROS management capacity in *Symbiodinium* sp. Remarkably, this upregulation persisted a week after a pulsed UV-B stress, suggesting that short-term stress can shape long-term survival strategies. This aligns with the observed increase in the *Symbiodinium* sp. to *Chlorella* sp. ratio over time postirradiation (Fig. 2*A*). Additionally, genes linked to growth and metabolism, such as those involved in ATPase activity, phosphorus metabolism, cytoskeleton organization, and DNA replication, were also upregulated in *Symbiodinium* sp. but downregulated in *Chlorella* sp. (*SI Appendix*, Fig. S7). Therefore, the differential ability of red lineage and green lineage to metabolize ROS not only dictates their immediate stress responses but also profoundly influences their long-term growth patterns and ecological succession.

Role of ROS in the Evolution of Red and Green Lineage Phytoplankton. To test the central hypothesis that physiological advantages observed over short laboratory timescales can scale up to become fundamental forces shaping macroevolutionary patterns, we compared the evolutionary trajectories of two phytoplankton lineages with paleoenvironmental turning points known to have triggered global increases in marine ROS. Fossil evidence reveals clear macroevolutionary patterns: Acritarchs, characteristic of the green lineage (32), dominated primary productivity in Paleozoic oceans (Fig. 5*A*). At the onset of the Mesozoic, however, a pronounced evolutionary radiation of red lineages occurred, as evidenced by extensive and continuous fossil records of calcite-armored coccolithophores (Fig. 5*B*) and organic-walled cyst-producing dinoflagellates (Fig. 5*C*). Our phylogenomic analysis (*SI Appendix*, Fig. S8), based on a 320-protein dataset from 136 taxa (33), aligns with these fossil trends, showing that major green lineage clades had diversified before the Mesozoic, whereas the red lineage, though equally ancient, diversified extensively during and after the Mesozoic. For instance, most major subgroups of *Myzozoa* radiated post-Paleozoic (*SI Appendix*, Fig. S8). The crown groups of red and green algae originated contemporaneously, dated to 959.7 Ma (95% HPD: 784.6 to 1,127.1) and 976.5 Ma (95% HPD: 854.7 to 1,092.9), respectively, confirming their parallel origins and long evolutionary histories. However, their diversification trajectories diverged sharply during the Mesozoic.

This evolutionary turnover aligns with a major turning point in Earth's environment (Fig. 5*D*). Although Paleozoic oceans were warm, they were characterized with low background levels of key ROS-inducing factors, including high-flux UV-B radiation and dissolved Fe(II). The environmental damage caused by the Siberian Traps enormous volcanic province, beginning in the late Paleozoic,

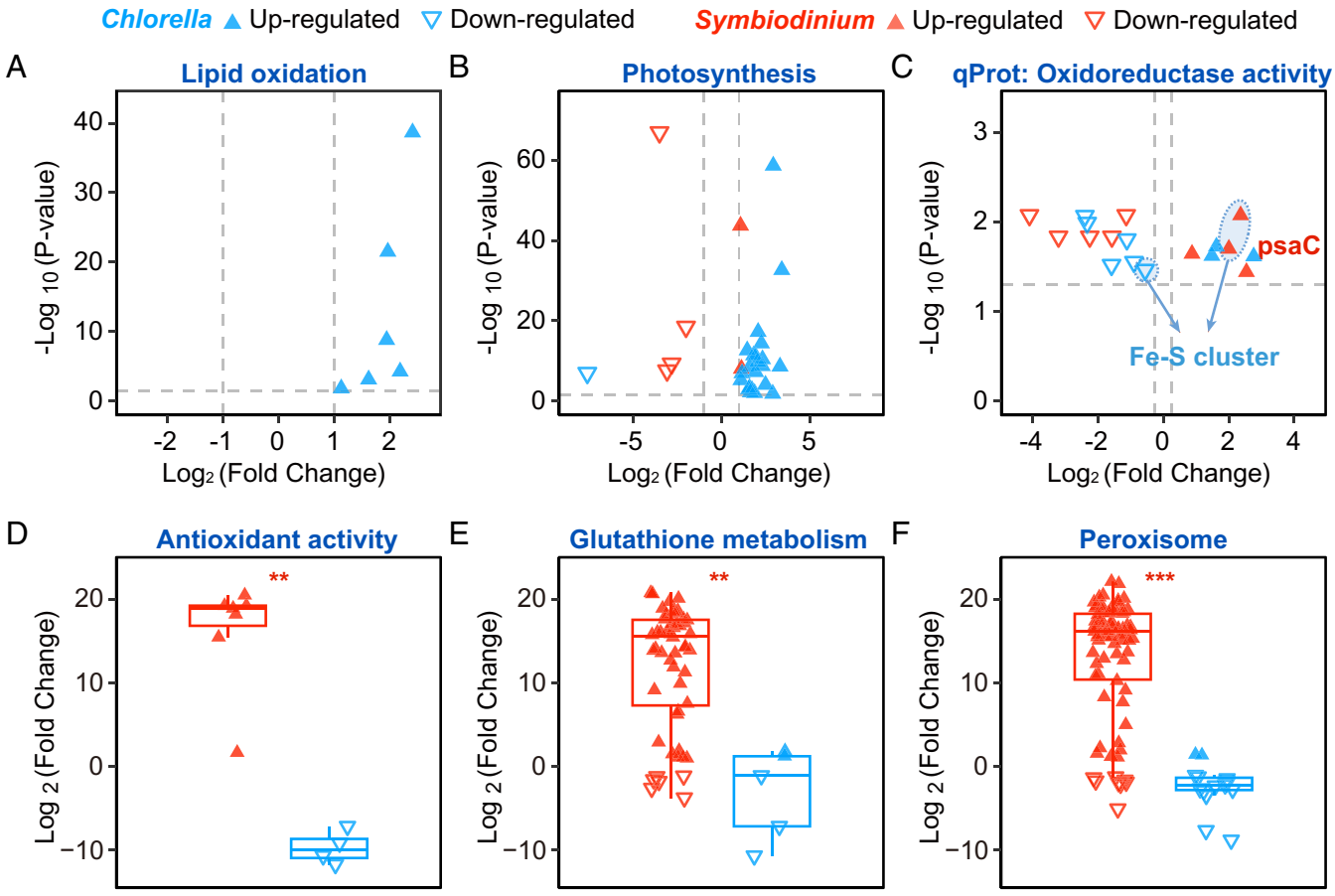

Fig. 4. Differential expressions of genes or proteins in *Chlorella* sp. (green lineage) and *Symbiodinium* sp. (red lineage) after UV-B radiation. (*A*) Lipid oxidation-related genes (GO: 0034440); (*B*) Photosynthesis-related genes (GO: 0015979); (*C*) Oxidoreductase activity-related proteins (GO: 0016491); (*D*) Antioxidant activity-related genes (GO: 0016209); (*E*) Glutathione metabolism-related genes (ko00480); (*F*) Peroxisome-related genes (ko04146). UV-B irradiation was applied at a dose of 66 kJ/m^2/d over a 10-h photoperiod. Groups (*A–C*) were assessed immediately after radiation, while groups (*D–F*) after 7 d of recovery following radiation. Data are from three biological replicates (N = 3). *P*-values were derived using the Wilcoxon rank-sum test with BH correction for multiple comparisons. Significance was represented as * for $P < 0.05$, and ** for $P < 0.01$, and *** for $P < 0.001$.

substantially altered worldwide marine biogeochemistry. Massive halogen emissions destroyed the ozone layer, drastically increasing the flux of lethal UV-B radiation (21), while global warming induced widespread marine anoxia that sustained high concentrations of Fe(II) (22). These factors, acting combined in oceans already warmed above 25 °C (20), could create a long-term, global high-ROS environment. This global high-ROS environment imposed a powerful selective pressure that enhanced the evolutionary consequences of the physiological differences between the two lineages. Our experimental results provide the mechanistic basis for this outcome: the superior ROS-scavenging capacity of the red lineage acted as a key adaptive trait that facilitated its ecological expansion and diversification in this new environment. The green lineage's relative physiological weakness limited its capacity to thrive.

Discussion

The shift from green to red lineage phytoplankton under environmental stresses reflects a fundamental evolutionary transition, one that not only reshaped marine primary productivity in the early Mesozoic but also reveals the central role of ROS as a physiological constraint and evolutionary driver. Our findings demonstrate that red lineage phytoplankton possess structural and metabolic features that confer enhanced resilience to ROS stress, allowing them to outcompete green lineage counterparts under specific environmental conditions, notably elevated UV-B radiation and Fe(II) levels (Fig. 6).

ROS as a Central Integrator of Environmental Stress. While prior studies have posited nutrient limitation, ocean redox state, or trace metal availability as key drivers of phytoplankton evolution (3, 6), these frameworks often lack a unifying physiological mechanism. ROS may act as a critical chain bridging different environmental stresses and the responses of different lives. As both a damaging agent and a signaling molecule, ROS translates environmental cues (e.g., UV-B, redox-active metals, temperature) into cellular stress responses (9, 41, 42). Importantly, our results demonstrate that only stressors capable of inducing substantial environmental ROS, such as UV-B and Fe(II) oxidation, correspond to red lineage dominance, whereas high CO_2 or nutrient shifts, which do not elevate environmental ROS levels, maintain green lineage advantage. The correlation between environmental ROS concentrations and lineage abundance, along with experimental manipulations using environmental ROS quenchers and donors, provides compelling evidence for a causal link. This supports the view that ROS acts not merely as a byproduct of stress but as a proximal selective force capable of reshaping community structure and long-term evolutionary trajectories.

Structural and Biochemical Mechanisms Underpinning ROS Tolerance. Red lineage phytoplankton resists ROS accumulation via multiple complementary mechanisms. Morphologically, they exhibit thicker cell walls, which function as a first line of defense against environmental ROS penetration. Biochemically, their EPS

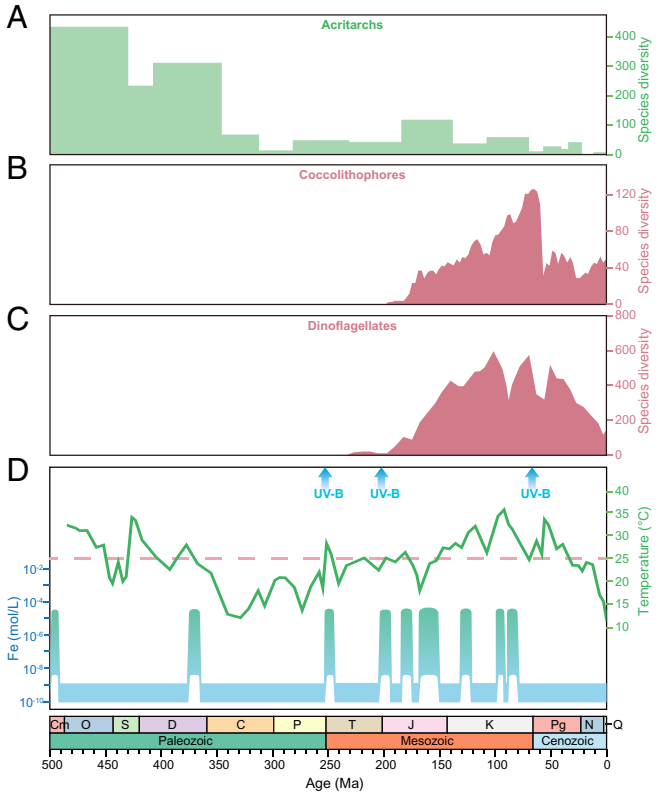

Fig 5. Coevolution of phytoplankton diversity and paleoenvironmental proxies during the Phanerozoic Eon. (*A*–*C*) Phanerozoic diversity trajectories of major phytoplankton groups based on the fossil record of (*A*) Acritarchs (representing the green lineage) (34), (*B*) Coccolithophores (35), and (*C*) Dinoflagellates (32). (*D*) Paleoenvironmental reconstructions. The green line shows the global SST, with the dashed line marking the 25 °C threshold. The lower blue bars indicate the concentration of dissolved ferrous iron [Fe(II)], and the blue arrows denote periods of increased UV-B radiation. Dissolved iron data are adapted from Song et al. (36), and temperature data are updated based on Judd et al. (37). Periods of elevated UV-B radiation are indicated, as suggested by previous studies (38–40).

are not only preserved but even enriched under UV-B stress, with sulfated polysaccharide content known to enhance free radical scavenging capacity (25, 43). In contrast, green lineage EPS is degraded under the same conditions, reducing their antioxidative shield. At the physiological level, transcriptomic and proteomic data reveal that red lineage cells adopt a low-energy, ROS-conserving strategy. By downregulating photosynthesis-related genes and upregulating components like *psaC* that stabilize the electron transport chain, they effectively minimize the generation of endogenous ROS from electron leakage. This contrasts with green lineage cells, which exhibit increased photosynthetic activity and lipid oxidation gene expression, leading to elevated endogenous ROS and membrane damage. The upregulation of antioxidant and repair genes in red lineage during post–stress recovery further highlights their long-term resilience and adaptive capacity. These differences underscore that ROS tolerance is not a single trait but a systems-level feature involving structural reinforcement, redox homeostasis, energy budgeting, and stress memory. Collectively, these features grant red lineage phytoplankton a competitive edge in oxidatively stressful environments.

From Short-Term Stress to Long-Term Evolution. Our phylogenetic and diversification analyses suggest that the lineage-specific physiological traits observed in our experiments have deep evolutionary roots. The antioxidant systems in Archaeplastida were inherited from the cyanobacterial primary endosymbiont, and the evolutionary origins of core antioxidant enzymes, such as superoxide dismutase, can be traced back to the Archean Eon. After inheriting this ancient molecular machinery, we propose that it was the long-term, divergent evolution of these defenses within each lineage over hundreds of millions of years that became the decisive factor in their later success. This deep-time differentiation, rather than simply the shared ancestry of the enzymes, likely explains why the red lineage was better equipped to thrive and ultimately displaced the green lineage when faced with the intensifying oxidative stress of the Paleozoic–Mesozoic transition. The concurrent rise in red lineage diversification rates and environmental ROS pressure [due to UV-B and Fe(II) increases] at the Paleozoic–Mesozoic transition strongly supports a causal relationship between environmental stress, ROS, and evolutionary selection. Crucially, our results reveal a threshold-like behavior in phytoplankton responses, with 25 °C and ~70 kJ/m^2/d UV-B emerging as inflection points for lineage shifts. This nonlinear response implies that evolutionary pressures under fluctuating stress regimes are not gradual but may be punctuated by tipping-point transitions when multiple stressors act synergistically to overwhelm cellular defenses.

From Deep Time to Climate Futures: ROS in Biota–Environment Coevolution. The centrality of ROS in stress response is not unique to phytoplankton. ROS also governs reproduction, growth, senescence, and inheritance in multicellular organisms, including animals and plants (44, 45). Therefore, ROS may represent a broadly conserved physiological mechanism driving evolutionary shifts across biological kingdoms. Its role as a mediator between short-term stress and long-term adaptation helps explain species turnover and ecological restructuring during critical periods in Earth's history, such as the Great Oxidation Event, the Cambrian explosion, and mass extinctions. By identifying ROS as a unifying physiological currency of environmental stress, our study provides a framework to reinterpret past biotic crises and radiations through a mechanistic lens. Furthermore, this framework is increasingly relevant in the Anthropocene, where global climate change, ozone depletion, and pollution elevate ROS-generating pressures across ecosystems.

In the present-day ocean, rising temperatures and UV-B exposure due to climate change and stratospheric ozone fluctuations may reconfigure phytoplankton community composition in ways reminiscent of early Mesozoic transitions. Our global dataset analysis shows that the ecological thresholds identified in experiments (e.g., 25 °C, 70 kJ/m^2/d UV) are already being crossed in many tropical and subtropical regions. This raises the possibility that red lineage phytoplankton, often associated with harmful algal blooms or low-nutrient strategies, may expand their range and influence biogeochemical cycles, particularly carbon export and oxygen production. Moreover, the coupling of temperature with UV-B in amplifying ROS production suggests that climate warming could intensify oxidative pressures, even in the absence of further UV-B increases. These dynamics should be integrated into ecosystem models and marine biodiversity forecasts. Likewise, understanding ROS tolerance mechanisms could inform synthetic biology or aquaculture efforts aimed at engineering resilient primary producers under future stress regimes.

Conclusion

This study identifies ROS as a central physiological driver in the evolutionary transition from green to red lineage phytoplankton dominance during the early Mesozoic. Through integrative experiments, structural imaging, transcriptomics, proteomics, and

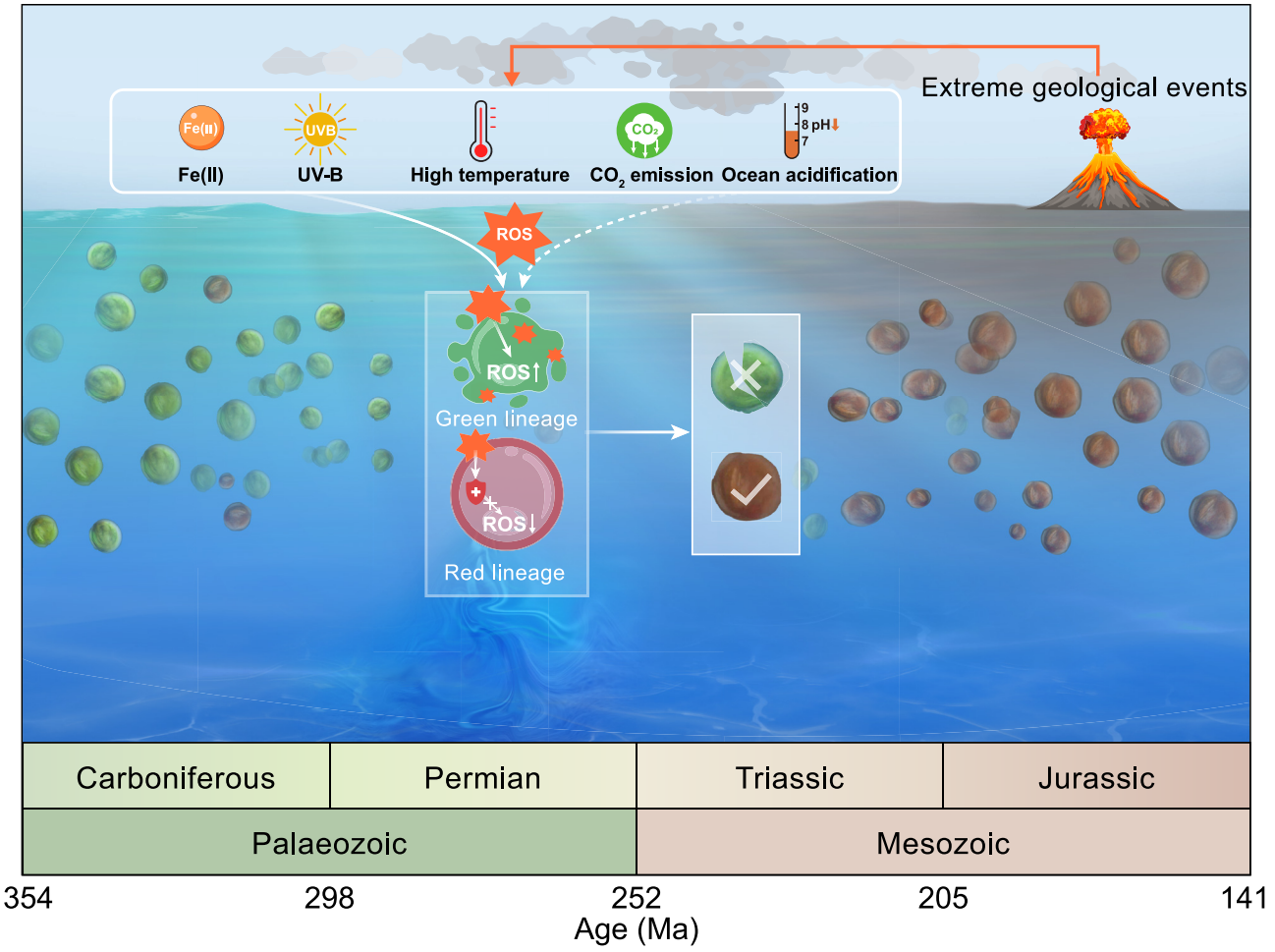

Fig. 6. Role of ROS in driving red lineage phytoplankton to displace green lineage phytoplankton during the Paleozoic.

phylogenetic analyses, we demonstrate that only environmental stressors capable of elevating environmental ROS beyond a critical threshold significantly induce shifts in phytoplankton communities. Red lineage phytoplankton have evolved mechanisms to defend against environmental ROS and limit endogenous ROS accumulation under stress. These traits conferred a selective advantage under the elevated UV-B radiation, increased Fe(II) availability, and warming temperatures characteristic of the early Mesozoic marine environment. By linking environmental factors, cellular stress responses, and evolutionary outcomes, our findings position ROS not merely as a byproduct of stress but as a key mediator of ecological and evolutionary change. This perspective offers predictive insights into modern environmental shifts, where rising ROS-inducing stressors may once again drive major transformations in primary producer communities and biodiversity patterns.

Materials and Methods

Cultivation Conditions. *Chlorella* sp., *Symbiodinium* sp., *C. meneghiniana*, *T. pseudonana*, *Dunaliella* sp., and *N. oceanica* were obtained from Shanghai Guangyu Biological Technology Co., Ltd. Notably, *Symbiodinium* sp. was isolated from Beibu Gulf, and *Chlorella* sp. from Zhanjiang, China. Prior to experiments, cells were cultured in F2 medium which contained artificial seawater salts (*SI Appendix*, Table S1) and was sterilized at 121 °C for 20 min. Cultures were maintained under continuous cool white fluorescent light at 3,200 lx with a 12-h light/dark cycle. Both strains were acclimated for at least 8 wk (4 transfers) before the experiments.

Chemicals. The primary reagents included humic acid sodium salt (HA, Technical Grade) purchased from Sigma-Aldrich, 2′,7′-dichlorodihydrofluorescein diacetate (DCFH-DA, >97%), disodium terephthalate (TPA, >99%), and p-hydroxybenzoic acid (hTPA, ≥99.5%), all purchased from Aladdin Industrial Corporation. Phosphate-buffered solution (PBS) was obtained from Biosharp (China). iFluorTM 647-Concanavalin A Conjugate was purchased from AAT Bioquest (USA). Other analytical-grade reagents were obtained from Sinopharm Chemical Reagent Co., Ltd. (China). Ultrapure water (18.2 MΩ cm) was produced using a Heal Force NW system.

Batch Experiments. For the control group, *Chlorella* sp. and *Symbiodinium* sp. were cultured in simulated seawater supplemented with 0.4 μM $Na_2HPO_4{\cdot}2H_2O$ and 6 μM $NaNO_3$ to provide inorganic phosphorus and nitrogen. To simulate the presence of organic matter in seawater, 0.3 mM HA and 3 μM Fe(III) (as $FeCl_3{\cdot}6H_2O$) were precomplexed in the dark for 12 h before addition to cultures. Cultures were maintained at 25 °C with shaking (150 rpm) and light intensity of 3,200 lx under a 12 h light/12 h dark cycle. Cell density, extracellular •OH concentration and intracellular ROS levels were regularly monitored throughout the growth period.

Effects of Environmental Conditions on Phytoplankton Growth. To simulate the high carbon dioxide (hypercapnic) conditions representative of the Late Permian to Early Triassic oceans, the composition of the aerating gas was modified. All gas mixtures were filter-sterilized by passing through a 0.22 μm nylon filter prior to use. The control group was aerated with a gas mixture of 30% O_2 and 0.04% CO_2, whereas the high-CO_2 treatment group received a mixture of 17% O_2 and 1% CO_2, with nitrogen as the balance gas. The initial pH of the culture medium was adjusted to 7.5 via this aeration to mimic oceanic conditions of that era. All other parameters were maintained identical to those of the control group.

The effects of UV-B irradiation on algal growth were assessed using a UV-B lamp (Sankyo, Japan) placed above the incubator (*SI Appendix*, Fig. S9). The irradiation intensity at the liquid surface in the quartz flask was measured with a UV-B irradiometer (Beijing Normal University, Beijing). Three different UV-B intensities were tested: 0, 3.1, and 6.6 kJ/m^2/h. UV-B exposure began 1 h after the start of each light period and ended 1 h before the dark phase, for a total exposure of 10 h. This resulted in total daily UV-B doses of 0, 31, and 66 kJ/m^2/d, respectively. All other culture conditions remained as in the control group.

Temperature effects were evaluated by incubating cultures at 35 °C, while maintaining other conditions identical to those in the UV-B treatment (25 °C), to assess the impact of elevated temperature on the growth of *Chlorella* sp. and *Symbiodinium* sp.

To assess Fe(II) oxidation effects, 0.1 mM Fe(II) (as $FeSO_4{\cdot}7H_2O$) was added to simulated seawater without HA and Fe(III) complexes. All other culture conditions remained consistent with the control group [0 mM Fe(II)].

The influence of different concentrations of nutrients was examined in culture media containing 0.04, 0.4, and 4 μM $Na_2HPO_4{\cdot}2H_2O$. To simulate marine environments under different metal conditions, the ratios of Fe, Mn, and Cu were adjusted. For high Fe-Mn conditions, 100 nM Fe(III) (as $FeCl_3{\cdot}6H_2O$), 2 nM Mn(II) (as $MnCl_2{\cdot}4H_2O$), 4 nM Cu(II) (as $CuSO_4{\cdot}5H_2O$), and 150 nM Na_2EDTA were added. For high Cu conditions, 10 nM Fe(III), 0.2 nM Mn(II), 40 nM Cu(II), and 150 nM Na_2EDTA were incorporated. No HA–Fe(III) complexes were introduced. Everything else was the same as the control, which contained 0.4 μM $Na_2HPO_4{\cdot}2H_2O$ and 6 μM $NaNO_3$. Cell density, extracellular •OH concentration, and intracellular ROS levels were monitored throughout the growth period.

Relative Proportion Changes of Mixed Phytoplankton under UV-B. Mixed algal cultures were established by combining two red lineage algae (*C. meneghiniana* and *T. pseudonana*) and two green lineage algae (*Dunaliella* sp. and *N. oceanica*). To satisfy the silicate requirements of the diatoms in the culture, 100 μM sodium silicate ($Na_2SiO_3{\cdot}9H_2O$) was added to the medium. The cultures were exposed to UV-B irradiation at an intensity of 66 kJ/m^2/d, with the irradiation schedule identical to that of the previous UV-B experiments. All other culture conditions were kept consistent with those of the control group. After 12 h of light cultivation, including 10 h of UV-B exposure, 2 mL samples were collected for cell counting to evaluate changes in the relative proportions of the mixed algae.

Correlation Analysis between Phytoplankton Species Richness and UV-B Radiation Intensity and Ocean Surface Temperature. Phytoplankton species selection was performed in accordance with Righetti (46). Field data were compiled from six major phyla, *Chlorophyta*, *Euglenozoa*, *Ochrophyta*, *Cryptophyta*, *Haptophyta*, and *Myzozoa*, representing the global distribution of eukaryotic plankton. Data sources included the Global Biodiversity Information Facility (GBIF; https://www.gbif.org), the Ocean Biogeographic Information System (OBIS; https://www.obis.org), and PHYTOBASE (47). In our dataset, for *Euglenozoa* only the classes *Euglenophyceae* and *Euglenoidea* (microalgae containing both chlorophyll a and b) were retained. For *Ochrophyta*, we restricted the selection to *Bacillariophyceae*, *Chrysophyceae*, *Pelagophyceae*, and *Raphidophyceae*. Within *Myzozoa*, only *Dinophyceae* were included. Additionally, within *Chlorophyta*, the entire class *Ulvophyceae* was excluded. Similarly, the phylum *Rhodophyta* was excluded, as this analysis is restricted to phytoplankton and most rhodophytes are benthic macroalgae. Data preprocessing excluded invalid records, including unclassified species, fossil or specimen records, entries without geographic coordinates, depth anomalies (depths <0 or >500 m), and terrestrial distributions. To retain only data from the open ocean, data from regions shallower than 200 m or with surface salinities below 20 were excluded using surface salinity data from the World Ocean Atlas (WOA, https://www.ncei.noaa.gov/products/world-ocean-atlas) 2023 and bathymetry from the National Oceanic and Atmospheric Administration (NOAA, https://www.ngdc.noaa.gov/mgg/global/relief/). Taxonomic information was retrieved through World Register of Marine Species (WoRMS, https://www.marinespecies.org/).

UV-B radiation data for the period from 1940 to 2023 were obtained from the European Centre for Medium-Range Weather Forecasts Reanalysis 5 (ERA5). Monthly average values were calculated and then further averaged to determine the mean UV-B intensity. Ocean surface temperature data were sourced from Bio-ORACLE (https://bio-oracle.org/) for the period 2000–2020 (48).

To explore the correlations between different environmental factors and species richness, we first split our study region into 1°×1° grid cells. For each grid cell, we calculated the total number of unique red lineage and green lineage species recorded, which serves as a proxy for lineage-wide diversity. We then took the logarithm of species richness data (ln) and used locally weighted scatterplot smoothing (LOESS) regression to create a nonlinear model describing association between species richness and relevant environmental factors.

Role of ROS in Relative Proportion Changes of Phytoplankton. To specifically remove the •OH, the most biologically destructive ROS generated in the reaction, a quenching experiment was performed. In the UV-B irradiation experiment, an additional 10 mM TPA was added to scavenge •OH radicals (49). After 24 h of cultivation, algal counts were measured.

To demonstrate the direct effect of ROS on algal proportions, 0, 0.5, and 2 mM H_2O_2 were respectively added to simulated seawater containing the two types of algae. HA and Fe(III) complexes were excluded from simulated seawater. All other conditions remained consistent with those of the control group. After 24 h of cultivation, algal counts and intracellular ROS levels were assessed.

Quantification of Algal Cell Densities. In an effort to measure the population densities of *Chlorella* sp. and *Symbiodinium* sp., composite samples were put in a phytoplankton counting chamber containing 400 individual squares in a volume of 0.1 mL. The chamber was then sealed with a cover glass and allowed to rest for a time to allow the cells to settle. A microscope (Leica DM2500, Germany) was then used to randomly select 54 squares and count *Chlorella* sp. and *Symbiodinium* sp. cells in these selected squares to facilitate overall cell densities.

Cell Observation. For morphological comparison of *Chlorella* sp. and *Symbiodinium* sp. under UV-B irradiance, cells were harvested at the end of the 10-h UV-B exposure period in the 0 and 66 kJ/m^2/d treatment groups. Cell suspensions were centrifuged at 8,000 rpm and fixed in 2.5% glutaraldehyde for 12 h. Fixed cells were washed three times (15 min each) in 0.1 M phosphate buffer (pH 7.2), then postfixed in 1% osmium tetroxide at room temperature for 2 h. After three more washes, samples were dehydrated in a graded ethanol series (30 to 100%). Dehydrated samples were sequentially infiltrated with acetone mixtures (2:1, 1:1) and pure epoxy resin at 37 °C. Samples were embedded in epoxy resin and polymerized at 60 °C for 48 h. Ultrathin sections (80 to 100 nm) were cut with a Leica EM UC7 ultramicrotome (Germany), double-stained with uranyl acetate and lead citrate (15 min each at room temperature), and viewed using a Hitachi HT7700 transmission electron microscope (Japan).

Extracellular •OH Measurement. Extracellular •OH was quantitated by utilizing a TPA probe (49). 2 mL sample was passed through a membrane filter with a porosity of a 0.22-μm nylon membrane followed by quenching any resultant •OH synthesis with methanol. •OH accumulation was quantified using a 10 mM TPA probe. hTPA formed was characterized with a Shimadzu LC-16C system comprising a fluorescence detector along with an HPLC. Separation was achieved using a C18 column (4.6 mm × 250 mm) with a mobile phase of 0.03% formic acid and 40% methanol (60:40, v). Fluorescence was measured at excitation and emission wavelengths of 250 nm and 410 nm, respectively. Total concentration of •OH was calculated through blank fluorescence subtraction along with a provided calibration factor along with a lower point of detection of 4 nM. By subtracting the calibration factor from the intensity of the blank fluorescence, the cumulative hTPA concentrations in various systems were calculated. Since fluorescence is too sensitive, the samples that were taken before reactions were utilized as the blanks. [hTPA]/35% was used to compute the cumulative •OH concentration. In the UV-B irradiation experiments, hTPA was susceptible to photolysis under UV-B exposure, so 10 mM benzoic acid (BA) was used as the probe instead. The cumulative concentration of •OH was measured using the transformation of benzoic acid to p-hydroxybenzoic acid (p-HBA) as a probe reaction (50). The concentration of *p*-HBA was quantified using an LC-15 C HPLC system (Shimadzu) equipped with a UV detector and a C18 column (4.6 × 250 mm). The cumulative •OH concentration was estimated based on the *p*-HBA concentration using a conversion factor of 5.87 (50).

Quantification of Intracellular ROS and Polysaccharides in EPS and Cell Wall. Intracellular ROS levels in *Chlorella* sp. and *Symbiodinium* sp. were measured using the fluorescent probe DCFH-DA (51). EPS and cell wall polysaccharides (α-D-mannosyl and α-D-glucosyl residues) were visualized using ConA-647 lectin. Algal cultures (3 mL, 4 × 10^5 cells/mL) were incubated in the

dark at 25 °C for 12 h before exposure to various environmental conditions (UV-B, temperature, H_2O_2, gas composition, phosphate, and metal ions). For the UV-B treatment group, cells were harvested at the end of the 10 h exposure period. For all other environmental treatments, cells were collected after 24 h of exposure. Harvested 24 h cultivation, cells were washed twice with PBS and stained with 20 μM DCFH-DA in darkness at 37 °C for 20 min. Following PBS washing, the same samples were incubated with 10 μg/mL ConA-647 for an additional 20 min at 37 °C in darkness, then washed twice with PBS. Stained cells were mounted on glass slides and imaged using a CLSM (Leica Stellaris 5, Germany). ROS fluorescence was detected at excitation/emission wavelengths of 488/525 nm, while ConA-647–labeled polysaccharides were visualized at 647/668 nm.

RNA Isolation and Sequencing. To clarify the functional processes involved in varied responses of both *Chlorella* sp. and *Symbiodinium* sp. to UV-B irradiation, transcriptome sequencing was performed for RNA samples collected in three different conditions: before irradiation, following exposure to UV-B for 10 h at doses of 0 and 66 kJ/m^2/d, and following UV-B exposure for 10 h with a culture period prolonged to 7 d. Total RNA was extracted based on Total RNA Extraction Kit (DP441, TIANGEN, China) instructions.

The transcriptome was sequenced by MegaGene in Guangzhou, China. RNA quality was evaluated using the Thermo Fisher Scientific NanoDrop One, in addition to the Agilent Technologies Agilent 4200 TapeStation and Agilent 2100 Bioanalyzer. Library preparation included mRNA enrichment with Oligo(dT) magnetic beads, fragmentation, cDNA synthesis, end repair, A-tailing, adapter ligation, size selection, and PCR amplification using AMPure XP beads for purification.

Libraries were sequenced on Illumina HiSeq 2500 (*Chlorella* sp.) and NovaSeq (*Symbiodinium* sp.) platforms. *Chlorella* sp. reads were mapped to a reference genome (GenBank: JBJHFK000000000), while *Symbiodinium* sp. reads underwent de novo assembly. Quality control was performed using fastp (52) with defined criteria for base quality and read length. Ribosomal RNA sequences were removed using Bowtie2 (53, 54) alignment against NCBI RefSeq and Rfam databases, with unaligned reads extracted using samtools (55, 56). Quality control results for *Chlorella* sp. and *Symbiodinium* sp. are presented in *SI Appendix*, Tables S2 and S3, respectively. For *Symbiodinium* sp., transcriptome assembly used Trinity followed by redundancy reduction with cd-hit. Transcripts were functionally annotated against GO and KEGG databases using diamond (57). For *Chlorella* sp., transcriptome assembly used StringTie (58) with the reference genome, generating and merging GTF files across samples. Differential expression analysis was conducted using DESeq2 (59), with differentially expressed genes defined by an adjusted *P*-value ≤ 0.05 and $|\log_2 FC| \geq 1$. The Benjamini–Hochberg (BH) method was applied for multiple testing correction. Functional annotation was followed against GO and KEGG databases to ascertain differentially expressed genes with respect to their biology.

Proteomic Analysis. Proteomic analysis was performed by MegaGene (Guangzhou, China) on mixed cultures of *Chlorella* sp. and *Symbiodinium* sp. 10 h after exposure to UV-B at 0 and 66 kJ/m^2/d. Proteins were extracted using 8 M urea with 10% protease inhibitor, followed by centrifugation at 14,100 × g for 20 min. Protein concentrations were determined by Bradford assay. For digestion, 100 μg protein per sample was reduced with 200 mM DTT, diluted with 25 mM ABC buffer, and digested with trypsin (1:50 ratio) overnight at 37 °C. Digested peptides were desalted using C18 columns before LC-MS/MS analysis.

Samples were measured on a Q Exactive HF-X mass spectrometer (Thermo Fisher Scientific) interfaced with an EASY nLC 1200 system. For the creation of spectra libraries, samples were fractioned and measured in DDA mode. For quantitation, the samples were measured in DIA mode with 42 variable windows of isolation. Data were processed using Spectronaut (v15.7, Biognosys) against UniProt *Chlorella desiccata* (UP000693320) and *Symbiodinium* sp. (UP000643038) proteome databases. Carbamidomethylation was set as fixed modification, while N-terminal acetylation and methionine oxidation were variable. A 1% FDR was applied for protein and precursor identifications. DEPs were identified on the basis of the *t* test with an adjusted *P*-value ≤ 0.05 and a fold change ≥ 1.2. Storey's q-value method was applied to adjust the *P*-values (60). Functional annotations were made according to GO and InterPro, and protein interactions were predicted using STRING-db. The proteomics data are available in the iProX database (project ID IPX0010202002).

Phylogenetic Tree and Molecular Clock Construction. The prealigned and trimmed sequence data for the 320-protein supermatrix were sourced from the study by Strassert et al. (33). This revised strategy differs from the original study in two critical aspects. First, we constrained the tree root with a uniform prior of 1.642 to 1.9 Ga (61, 62). This narrower range is consistent with recent multigene analyses that place crown Eukarya younger than 1.9 Ga and avoids the problematic deep divergences resulting from the broader 1.6 to 3.2 Ga prior used previously (62). Second, we updated the set of six internal constraints (*SI Appendix*, Table S4). This includes the integration of a revised, more recent age for crown-group *Chlorophyta* and the use of a well-established minimum constraint for *Rhodophyta*, thereby avoiding a more controversial 1.6 Ga calibration for that node. A maximum-likelihood (ML) phylogenetic tree was constructed using IQ-TREE v3.0.1 (63). The analysis was conducted using the LG+C60+G+F model, and branch support was assessed with 1000 ultrafast bootstrap replicates.

Bayesian molecular dating was performed using MCMCTree within the PAML package (v4.9j) (64). Six calibration points were used in all molecular clock analyses (*SI Appendix*, Table S4). We assumed a uniform birth–death tree prior and ran the analysis with an autocorrelated relaxed clock model (clock = 3). The dataset was analyzed as a single partition under the LG+G substitution model. The prior for the mean substitution rate (rgene_gamma) was set using a gamma distribution ($\alpha = 2$, $\beta = 51.03$), with the mean rate estimated using codeml. The rate drift parameter prior (sigma2_gamma) was set to ($\alpha = 2$, $\beta = 2$) to account for considerable rate heterogeneity across lineages. Two independent MCMC chains were run, each for 22,000,000 generations, with the first 2,000,000 discarded as burn-in. Chain convergence was assessed in Tracer v1.7.2, confirming that all parameters reached an effective sample size greater than 200.

Statistics. Unless otherwise indicated, all experiments were performed with $n = 4$ replicates. Transcriptomic and proteomic analyses included three biological replicates. Statistical analyses included weighted linear regression (Fig. 2*B*), two-tailed *t* tests (Fig. 2 *C* and *D*), and the Wilcoxon rank-sum test with BH correction for multiple comparisons (Fig. 4 *D*–*F*).

Data, Materials, and Software Availability. RNA-Seq data have been deposited in the NCBI SRA (accession nos. PRJNA1184191 and PRJNA1184135) (65, 66). Proteomics data have been deposited in the ProteomeXchange Consortium (accession no. PXD072317) (67). Previously published data were used for this work (33, 47). All other data are included in the article and/or *SI Appendix*.

ACKNOWLEDGMENTS. This work was supported by the National Natural Science Foundation of China (grant Nos. 42025703 and 42277072), National Key R&D Program of China (Grant No. 2023YFF0804000), and the Graduate Student Project from the Hubei Research Center for Basic Disciplines of Earth Sciences (grant No. HRCES-202414). We would like to express our sincere gratitude to Prof. Chen-Yang Cai from the Nanjing Institute of Geology and Palaeontology, Chinese Academy of Sciences, for his valuable suggestions on phylogenetic tree analysis. We also thank Mega Gene (Guangzhou, China) for their technical support with transcriptome and proteome experiments.

Author affiliations: [a]State Key Laboratory of Geomicrobiology and Environmental Changes, China University of Geosciences, Wuhan 430078, China; and [b]Department of Geosciences, University of Tübingen, Tübingen 72074, Germany

1. C. B. Field, M. J. Behrenfeld, J. T. Randerson, P. G. Falkowski, Primary production of the biosphere: Integrating terrestrial and oceanic components. *Science* **281**, 237–240 (1998).
2. R. B. Kodner, A. Pearson, R. E. Summons, A. H. Knoll, Sterols in red and green algae: Quantification, phylogeny, and relevance for the interpretation of geologic steranes. *Geobiology* **6**, 411–420 (2008).
3. P. G. Falkowski *et al.*, The evolution of modern eukaryotic phytoplankton. *Science* **305**, 354–360 (2004).
4. R. E. Martin, T. Servais, Did the evolution of the phytoplankton fuel the diversification of the marine biosphere? *Lethaia* **53**, 5–31 (2020).
5. R. Martin, A. Quigg, Evolving phytoplankton stoichiometry fueled diversification of the marine biosphere. *Geosciences* **2**, 130–146 (2012).
6. M. E. Katz, Z. V. Finkel, D. Grzebyk, A. H. Knoll, P. G. Falkowski, Evolutionary trajectories and biogeochemical impacts of marine eukaryotic phytoplankton. *Annu. Rev. Ecol. Evol. Syst.* **35**, 523–556 (2004).

7. A. Quigg *et al.*, The evolutionary inheritance of elemental stoichiometry in marine phytoplankton. *Nature* **425**, 291–294 (2003).
8. L. K. Medlin, The permian-triassic mass extinction forces the radiation of the modern marine phytoplankton. *Phycologia* **50**, 684–693 (2011).
9. P. García-Caparrós *et al.*, Oxidative stress and antioxidant metabolism under adverse environmental conditions: A review. *Bot. Rev.* **87**, 421–466 (2021).
10. E. M. White, P. P. Vaughan, R. G. Zepp, Role of the photo-Fenton reaction in the production of hydroxyl radicals and photobleaching of colored dissolved organic matter in a coastal river of the southeastern United States. *Aquat. Sci.* **65**, 402–414 (2003).
11. B. Halliwell, J. M. C. Gutteridge, *Free Radicals in Biology and Medicine* (Oxford University Press, 2015).
12. L. N. Sun, J. G. Qian, N. V. Blough, K. Mopper, Insights into the photoproduction sites of hydroxyl radicals by dissolved organic matter in natural waters. *Environ. Sci. Technol. Lett.* **2**, 352–356 (2015).
13. M. Fujii, E. Otani, Photochemical generation and decay kinetics of superoxide and hydrogen peroxide in the presence of standard humic and fulvic acids. *Water Res.* **123**, 642–654 (2017).
14. H. Sies, R. J. Mailloux, U. Jakob, Fundamentals of redox regulation in biology. *Nat. Rev. Mol. Cell Biol.* **25**, 701–719 (2024).
15. R. Mittler, S. Vanderauwera, M. Gollery, F. Van Breusegem, ROS signaling: The new wave? *Trends Plant Sci.* **16**, 300–309 (2011).
16. H. Sies, V. V. Belousov, N. S. Chandel, M. J. Davies, D. P. Jones, Defining roles of specific reactive oxygen species (ROS) in cell biology and physiology. *Nat. Rev. Mol. Cell Biol.* **23**, 499–515 (2022).
17. C. H. Foyer, G. Noctor, Oxidant and antioxidant signalling in plants: A re-evaluation of the concept of oxidative stress in a physiological context. *Plant Cell Environ.* **28**, 1056–1071 (2005).
18. Y. Zheng, J. Sun, Z. Luo, Y. Li, Y. Huang, Emerging mechanisms of lipid peroxidation in regulated cell death and its physiological implications. *Cell Death Dis.* **15**, 859 (2024).
19. M. Khademian, J. A. Imlay, How microbes evolved to tolerate oxygen. *Trends Microbiol.* **29**, 428–440 (2021).
20. Y. Wu *et al.*, Six-fold increase of atmospheric pCO2 during the Permian-Triassic mass extinction. *Nat. Commun.* **12**, 2137 (2021).
21. D. J. Beerling, M. Harfoot, B. Lomax, J. A. Pyle, The stability of the stratospheric ozone layer during the end-Permian eruption of the Siberian Traps. *Philos. Trans. A Math. Phys. Eng. Sci.* **365**, 1843–1866 (2007).
22. C. Mettam *et al.*, High-frequency fluctuations in redox conditions during the latest Permian mass extinction. *Palaeogeogr. Palaeoclimatol. Palaeoecol.* **485**, 210–223 (2017).
23. Z. Markina, T. Orlova, Ultrastructural changes in marine microalgae from different taxonomic groups during batch cultivation. *Russ. J. Mar. Biol.* **45**, 202–210 (2019).
24. O. Spain, C. Funk, Detailed characterization of the cell wall structure and composition of Nordic green microalgae. *J. Agric. Food Chem.* **70**, 9711–9721 (2022).
25. R. Xiao, Y. Zheng, Overview of microalgal extracellular polymeric substances (EPS) and their applications. *Biotechnol. Adv.* **34**, 1225–1244 (2016).
26. H. Yin, L. Xu, N. A. Porter, Free radical lipid peroxidation: Mechanisms and analysis. *Chem. Rev.* **111**, 5944–5972 (2011).
27. S. Khorobrykh, V. Havurinne, H. Mattila, E. Tyystjarvi, Oxygen and ROS in photosynthesis. *Plants (Basel)* **9**, 91 (2020).
28. N. Fischer, M. Hippler, P. Setif, J. P. Jacquot, J. D. Rochaix, The PsaC subunit of photosystem I provides an essential lysine residue for fast electron transfer to ferredoxin. *EMBO J.* **17**, 849–858 (1998).
29. Y. Lima-Melo, M. Kılıç, E. M. Aro, P. J. Gollan, Photosystem I inhibition, protection and signalling: Knowns and unknowns. *Front. Plant Sci.* **12**, 791124 (2021).
30. C. Mazza, E. Gabriel, M. Mello, Oxidative stress: Cause mechanisms and defense agents. *Cardiol. Vasc. Res.* **3**, 1–5 (2019).
31. M. R. Gauthier, G. N. A. Senhorinho, J. A. Scott, Microalgae under environmental stress as a source of antioxidants. *Algal Res.* **52**, 102104 (2020).
32. L. E. Stover *et al.*, "Mesozoic-Tertiary dinoflagellates, acritarchs and prasinophytes" in *Palynology: Principles and Applications*, J. Jansonius, D. C. McGregor, Eds. (American Association of Stratigraphic Palynologists Foundation, 1996), pp. 641–750.
33. J. F. H. Strassert, I. Irisarri, T. A. Williams, F. Burki, A molecular timescale for eukaryote evolution with implications for the origin of red algal-derived plastids. *Nat. Commun.* **12**, 1506 (2021).
34. H. Tappan, A. R. Loeblich, Evolution of the oceanic plankton. *Earth Sci. Rev.* **9**, 207–240 (1973).
35. P. R. Bown, J. A. Lees, J. R. Young, "Calcareous nannoplankton evolution and diversity through time" in *Coccolithophores: From Molecular Processes to Global Impact*, H. R. Thierstein, J. R. Young, Eds. (Springer, Berlin, 2004), pp. 481–508.
36. H. Song *et al.*, The onset of widespread marine red beds and the evolution of ferruginous oceans. *Nat. Commun.* **8**, 399 (2017).
37. E. J. Judd *et al.*, A 485-million-year history of earth's surface temperature. *Science* **385**, eadk3705 (2024).
38. S. Lindström *et al.*, Volcanic mercury and mutagenesis in land plants during the end-Triassic mass extinction. *Sci. Adv.* **5**, eaaw4018 (2019).
39. C. G. Bardeen, R. R. Garcia, O. B. Toon, A. J. Conley, On transient climate change at the Cretaceous–Paleogene boundary due to atmospheric soot injections. *Proc. Natl. Acad. Sci. U.S.A.* **114**, E7415–E7424 (2017).
40. F. Liu *et al.*, Dying in the sun: Direct evidence for elevated UV-B radiation at the end-Permian mass extinction. *Sci. Adv.* **9**, eabo6102 (2023).
41. Q. Dai, B. Yan, S. Huang, X. Liu, S. Peng, Response of oxidative stress defense systems in rice (Oryza sativa) leaves with supplemental UV-B radiation. *Physiol. Plant.* **101**, 301–308 (1997).
42. A. A. Cherkasov, R. A. Overton Jr., E. P. Sokolov, I. M. Sokolova, Temperature-dependent effects of cadmium and purine nucleotides on mitochondrial aconitase from a marine ectotherm, Crassostrea virginica: A role of temperature in oxidative stress and allosteric enzyme regulation. *J. Exp. Biol.* **210**, 46–55 (2007).
43. Q. Zhong *et al.*, The antioxidant activity of polysaccharides derived from marine organisms: An overview. *Mar. Drugs* **17**, 668 (2019).
44. D. K. Dowling, L. W. Simmons, Reactive oxygen species as universal constraints in life-history evolution. *Proc. R. Soc. B* **276**, 1737–1745 (2009).
45. A. Mhamdi, F. Van Breusegem, Reactive oxygen species in plant development. *Development* **145**, dev164376 (2018).
46. D. Righetti, M. Vogt, N. Gruber, A. Psomas, N. E. Zimmermann, Global pattern of phytoplankton diversity driven by temperature and environmental variability. *Sci. Adv.* **5**, eaau6253 (2019).
47. D. Righetti, M. Vogt, N. E. Zimmermann, M. D. Guiry, N. Gruber, PHYTOBASE: A global synthesis of open ocean phytoplankton occurrences. *PANGAEA* (2019).
48. J. Assis *et al.*, Bio-ORACLE v3.0. Pushing marine data layers to the CMIP6 Earth System Models of climate change research. *Ecol. Lett.* **33**, e13813 (2024).
49. S. E. Page, W. A. Arnold, K. McNeill, Terephthalate as a probe for photochemically generated hydroxyl radical. *J. Environ. Monit.* **12**, 1658–1665 (2010).
50. X. Zhou, K. Mopper, Determination of photochemically produced hydroxyl radicals in seawater and freshwater. *Mar. Chem.* **30**, 71–88 (1990).
51. C. P. LeBel, H. Ischiropoulos, S. C. Bondy, Evaluation of the probe 2', 7'-dichlorofluorescin as an indicator of reactive oxygen species formation and oxidative stress. *Chem. Res. Toxicol.* **5**, 227–231 (1992).
52. S. Chen, Y. Zhou, Y. Chen, J. Gu, fastp: An ultra-fast all-in-one FASTQ preprocessor. *Bioinformatics* **34**, i884–i890 (2018).
53. B. Langmead, S. L. Salzberg, Fast gapped-read alignment with Bowtie 2. *Nat. Methods* **9**, 357–359 (2012).
54. B. Langmead, C. Wilks, V. Antonescu, R. Charles, Scaling read aligners to hundreds of threads on general-purpose processors. *Bioinformatics* **35**, 421–432 (2019).
55. P. Danecek *et al.*, Twelve years of SAMtools and BCFtools. *Gigascience* **10**, giab008 (2021).
56. H. Li *et al.*, The sequence alignment/map format and SAMtools. *Bioinformatics* **25**, 2078–2079 (2009).
57. B. Buchfink, K. Reuter, H. G. Drost, Sensitive protein alignments at tree-of-life scale using DIAMOND. *Nat. Methods* **18**, 366–368 (2021).
58. M. Pertea *et al.*, StringTie enables improved reconstruction of a transcriptome from RNA-seq reads. *Nat. Biotechnol.* **33**, 290–295 (2015).
59. M. I. Love, W. Huber, S. Anders, Moderated estimation of fold change and dispersion for RNA-seq data with DESeq2. *Genome Biol.* **15**, 550 (2014).
60. J. D. Storey, R. Tibshirani, Statistical significance for genomewide studies. *Proc. Natl. Acad. Sci. U.S.A.* **100**, 9440–9445 (2003).
61. L. A. Riedman, S. M. Porter, M. A. Lechte, A. Santos, G. P. Halverson, Early eukaryotic microfossils of the late Palaeoproterozoic Limbunya Group, Birrindudu Basin, northern Australia. *Pap. Palaeontol.* **9**, e1538 (2023).
62. H. C. Betts *et al.*, Integrated genomic and fossil evidence illuminates life's early evolution and eukaryote origin. *Nat. Ecol. Evol.* **2**, 1556–1562 (2018).
63. L. T. Nguyen, H. A. Schmidt, A. von Haeseler, B. Q. Minh, IQ-Tree: A fast and effective stochastic algorithm for estimating maximum-likelihood phylogenies. *Mol. Biol. Evol.* **32**, 268–274 (2015).
64. Z. Yang, PAML 4: Phylogenetic analysis by maximum likelihood. *Mol. Biol. Evol.* **24**, 1586–1591 (2007).
65. Y. Zhao, RNA-seq of Chlorella sp. NCBI Sequence Read Archive. https://www.ncbi.nlm.nih.gov/bioproject/PRJNA1184191. Deposited 9 November 2024.
66. Y. Zhao, RNA-seq of Symbiodinium sp. NCBI Sequence Read Archive. https://www.ncbi.nlm.nih.gov/bioproject/PRJNA1184135. Deposited 9 November 2024.
67. Y. Zhao, Proteomics analysis of co-cultured Chlorella sp. and Symbiodinium sp. ProteomeXchange Consortium. http://proteomecentral.proteomexchange.org/cgi/GetDataset?ID=PXD072317. Deposited 22 December 2025.